Research Article

Nano Research
2022, 15(7): 6184–6191

ISSN 1998-0124 CN 11-5974/O4
https://doi.org/10.1007/s12274-022-4275-9

Synthesis of carbon nanotubes-supported porous silicon microparticles in low-temperature molten salt for high-performance Li-ion battery anodes

Qianliang Zhang[1], Baojuan Xi[1] (✉), Weihua Chen[2], Jinkui Feng[3], Yitai Qian[1], and Shenglin Xiong[1] (✉)

[1] *Key Laboratory of Colloid and Interface Chemistry, Ministry of Education, School of Chemistry and Chemical Engineering, State Key Laboratory of Crystal Materials, Shandong University, Jinan 250100, China*
[2] *Key Laboratory of Material Processing and Mold of Ministry of Education, Zhengzhou University, Zhengzhou 450001, China*
[3] *Key Laboratory for Liquid-Solid Structural Evolution & Processing of Materials, Ministry of Education, School of Materials Science and Engineering, Shandong University, Jinan 250061, China*

Received: 5 January 2022 / **Revised:** 18 February 2022 / **Accepted:** 27 February 2022

ABSTRACT

Silicon-based materials has attracted attention as a promising candidate for lithium-ion batteries (LIBs) with high energy density. However, severe volume variation, pulverization, and poor conductivity hindered the development of Si based materials. In this study, porous Si microparticles supported by carbon nanotubes (p-Si/CNT) are fabricated through simple molten salt assisted dealloying process at low temperature followed by acid treatment. The $ZnCl_2$ molten salt not only provides the liquid environment to enhance the reaction, but also participates the dealloying process and works as template for porous structure when removes by acid treatment. Additionally, distribution of defect sites in CNTs also increases after molten salt process. Density function theory (DFT) calculations further prove the defects could improve the adsorption of Li^+. The participation of CNTs can also contribute to the reaction kinetics and retain the integrity of the electrode. As expected, the p-Si/CNT anode manifests enhanced lithium-storage performance in terms of superior cycling stability and good rate capability. The p-Si/CNT//$LiCoO_2$ full cell assembly further demonstrates its potential as a prospective anode for high-performance LIBs.

KEYWORDS

porous Si microparticles, carbon nanotubes, molten salt, lithium-ion batteries

1 Introduction

In the past decades, lithium-ion batteries (LIBs) have been attracting a great deal of attention as energy storage devices for portable electronic devices, electric vehicles (EVs), hybrid electric vehicles (HEVs), and grid-scale storage [1]. Despite the energy density of LIBs has increased during the past decades, these applications put forward a growing demand of higher specific energy density and power density of LIBs. Currently, commercial graphite anodes indeed limit the energy density of LIBs due to its low theoretical reversible capacities (372 $mAh{\cdot}g^{-1}$) [2, 3]. Many efforts have been made to explore anode materials with high capacities, such as silicon based materials, phosphorus based materials, and modified lithium metallic anodes [4–9]. Silicon is widely considered as one of the most promising candidate to replace graphite due to its high abundance, high theoretical specific capacity (3,579 $mAh{\cdot}g^{-1}$), and comparable working potential (< 0.5 V vs. Li^+/Li) [10–13]. Nonetheless, the alloying reactions of Si and Li often cause a large volume expansion (~ 300%), resulting in pulverization of the anode structure and excess formation of a solid electrolyte interface (SEI) on the surface of Si particles. The concomitant and continuous consumption of lithium results in subsequent reduction in capacity during lithiation/delithiation [14–16]. Conventionally, the pulverization issue of silicon was addressed by decreasing the size of silicon to the nanoscale [17, 18]. However, a main drawback of nanosized silicon is the high surface area, which may lead to low tap density of the electrode and the low volumetric energy density, further hindering the practical applications.

In order to improve the tap density with the considerations of pulverization inhibition, three-dimensional (3D) porous Si materials in microscale have attracted considerable interest as they exhibit both high gravimetric and high volumetric energy densities [19]. The abundant pores inside have been proved to accommodate a large induced mechanical strain due to the expansion of lithiation process [20]. Porous silicon was commonly synthesized by etching Si based alloys [21–23]. However, the applications of porous silicon anode were still hindered by the poor conductivity, tremendous aggregation, and excess formation of SEI due to the high surface area of porous silicon. To address these issues, carbon materials were widely applied, since the carbon based materials can not only enhance the conductivity of the electrode, but also buffer the volumetric expansion and help keep the integrity of electrode relying on its flexibility and mechanical stability [24]. Various porous Si/C composites were reported with enhanced performances. For instance, An et al. reported a nanoporous silicon@carbon composite through CO_2

Address correspondence to Baojuan Xi, baojuanxi@sdu.edu.cn; Shenglin Xiong, chexsl@sdu.edu.cn

assisted dealloying process, suggesting a reversible capacity of 1,093 mAh·g^{-1} and a capacity retention of 86.3% after 2,000 cycles at 5 A·g^{-1} [25]. Chae et al. fabricated a microsized nanoprous Si protected by pitch derived carbon, which exhibited a capacity retention of 80% after 450 cycles in full cells [26]. Huang et al. demonstrated porous Si/C composite by the self-assemble process of nano silicon particles and phenolic resin, which gave a capacity retention of 1,526 mAh·g^{-1} after 100 cycles at a current density of 0.25 C [27]. However, these porous Si/C based composites involve complicated and inefficient synthesis process. Furthermore, some reactions require high temperature during the dealloying reactions, which may require high energy consumption and may also result in the formation of inactive SiC [28].

Inspired by the strong mechanical property of carbon nanotubes (CNTs) [29, 30], we conceived the preparation of nanoporous silicon microparticles supported by carbon nanotubes (denoted as p-Si/CNT) by low-temperature molten salt process as an anode material for LIBs. Porous silicon microparticles with abundant three-dimentional (3D) interconnected pore tunnels were fabricated by a dealloying strategy with the assistance of $ZnCl_2$. It not only worked as the medium of molten salt at low temperature (m.p. 283 °C), but also participated in the dealloying reaction of Mg_2Si and can be removed as a porous template. Subsequently, the CNTs uniformly distributed around porous silicon and formed interconnected framework, which addressed the issues of porous silicon particles. Additionally, more defects in CNTs were also observed after the molten salt process, which also elevated the electrochemical kinetics of Li ions. More importantly, no inactive SiC phase formed due to the low temperature of the molten salt process. The as-prepared p-Si/CNT delivers a good reversible capacity of 796.6 mA mAh·g^{-1} after 100 cycles at 500 mA·g^{-1} in half cell as well as a reversible capacity of 94.3 mAh·g$^{-1}_{cathode}$ at current density of 1 C after 200 cycles p-Si/CNT//$LiCoO_2$ full cell, further confirming the promising potential in the application as high-capacity anodes for LIBs.

2 Experimental

2.1 Materials

Industrial multiwalled CNTs and micron-sized silicon particles were purchased from Aladdin Chemical Reagent Co., Ltd (China). $ZnCl_2$, magnesium powder, hydrochloric acid (HCl) and hydrofluoric acid (HF) were purchased from Sinopharm Chemical Reagent Co., Ltd (China). All the materials were used without any further treatment.

2.2 Synthesis of Mg_2Si microparticles

The synthesis of Mg_2Si microparticles was based on our previously reported work [31]. In a typical synthesis process, 2.8 g of commercial Si microparticles and 5 g of Mg powder were mixed and added into a 20 mL stainless autoclave before sealed. The molar ratio of Si to Mg was 1:2.1 with the slight excess of Mg (5%), making sure the complete reduction of Si into Mg_2Si. Subsequently, the autoclave was maintained at 500 °C for 10 h and cooled to room temperature and the resulting dark blue Mg_2Si microparticles were collected for the following use.

2.3 Synthesis of p-Si/CNT

In a typical process, 1.2 g of as-obtained Mg_2Si powder and 0.6 g CNT powder were placed in an agate ball milling jar. Then the milling jar was loaded in a planetary ball mill (Nanda QM-3SP04) and run for 2 h at a speed of 200 rpm. Then, the mixture and 5.0 g of $ZnCl_2$ powder were transferred into a 20 mL stainless-steel autoclave. In order to prevent the affect from O_2 and H_2O, the above transferring procedures were carried out in an argon filled glove box. The autoclave was then sealed immediately and heated in a muffle furnace at 300 °C for 10 h with a heating rate of 5 °C·min^{-1}. After the autoclave cooling down to room temperature naturally, the product was collected and rinsed with 2 mol·L^{-1} HCl, deionized water, and anhydrous ethanol for three times, respectively. Finally, the products were further immersed in diluted HF for another 10 min and dried in vacuum oven at 60 °C for 12 h. As reference, Si/CNT was prepared by directly mixing the commercial bulk Si and CNT directly without any further process.

2.4 Materials characterizations

The morphology and microstructure of as-obtained materials were investiaged by field-emission scanning electron microscope (FESEM, Zeiss Gimni-300), field-emission transmission electron microscope (FETEM, JEOL JEM-ARM 200F), X-ray diffractometer (XRD, Bruker D8 Advance, Cu Kα radiation, λ = 1.5418 Å), X-ray photoelectron spectroscopy (XPS, Thermo ESCALAB 250Xi), Raman spectrum (LabRAM HR800 spectrometer with the laser of 632 nm wavelength), nitrogen adsorption and desorption isotherm (Micromeritics ASAP-2020HD88), Toledo thermogravimetric analysis (TGA) SDTA851 thermal analyzer, and a surface area analyzer (Micromeritics ASAP 2460).

2.5 Electrochemical measurements

Electrochemical properties of p-Si/CNT and Si/CNT were evaluated by CR2016 type coin cells. For half cells, the working electrode was prepared by mixing the active material, acetylene black, and sodium alginate binder in a weight ratio of 7:2:1 with distilled water to form a homogeneous slurry. The as-prepared slurry was then uniformly pasted on a copper foil, followed by drying in a vacuum oven at 60 °C overnight. The working electrode was pressed with a roller press and punched into circular disc with the diameter of 12 mm. The mass loading of active material was about 0.8–1.2 mg·cm^{-2}. The cells were assembled in a glove box filled with Ar (Mikurouna, O_2 < 0.1 ppm, H_2O < 0.1 ppm) with metallic lithium foil as the anode, microporous polypropylene membrane (celgard 2400) as the separator, and 1.0 M $LiPF_6$ in ethylene carbonate (EC) and dimethyl carbonate (DEC) (v/v 1:1) with 5% fluoroethylene carbonate (FEC) content as the electrolyte. The cells were tested on a LAND CT2001A instrument with a potential range of 0.01–1.5 V vs. Li^+/Li after being aged for at least 6 h. Cyclic voltammetry (CV) was performed with a scanning rate of 0.1 mV·s^{-1} and a cutoff voltage between 0.01 and 1.5 V. Electrochemical impedance spectroscopy (EIS) was measured at a voltage of 10 mV with a frequency range between 0.01 and 100 kHz. Both CV and EIS measurements were carried out on the electrochemistry workstation (CHI660D).

2.6 Electrochemical measurements of p-Si/CNT full cell

The full cell was investigated with commercial $LiCoO_2$ (LCO) as the cathode and p-Si/CNT as the anode with the potential range of 2.5–4.2 V vs. Li^+/Li. The cathode was prepared by mixing commercial $LiCoO_2$ powder, acetylene black and polyvinylidene fluoride (PVDF) binder with a weight ratio of 7:2:1 in the N-methyl-pyrrolidone (NMP) as dispersant. The mixture was then mixed well to form a homogeneous slurry and paste on the Al foil and then dried in the vacuum oven at 110 °C overnight. Al foil with active material was then pressed with a roller press and cut into circular wafer with the diameter of 10 mm. The assembly process of the full-cell is the same as that of the half cell. The anode used in full cell analysis was prelithiated for 3 cycles and the anode was designed with an excess capacity of 10% over the cathode.

2.7 Density functional theory (DFT) calculations

DFT has been developed in the Vienna *ab-initio* simulation package (VASP) to get the result of first-principle calculations [32, 33]. The calculations were performed with projector augmented wave (PAW) method and the Perdew-Burke-Ernzerhof (PBE) from generalized gradient approximation (GGA) for exchange and correlation [34, 35]. In the process of convergence optimization, an energy cut-off of 400 eV and a 2 × 2 × 1 Monkhorst–Pack *k*-mesh grid were set for the as-constructed 5 × 5 graphene supercell [36]. The force tolerance for all atoms change was set to 10^{-5} eV, and 0.01 eV·Å^{-1} for maximum residual force. The physical van der Waals interaction was represented via the optB86b-vdW functional, which clearly contributes to the absorb energy and optimization calculations.

3 Results and discussion

The synthesis process of p-Si/CNT was schematically illustrated in Fig. 1(a). Mg_2Si precursor was initially fabricated according to a specific procedure reported via the alloying reaction of Mg and Si (Fig. S1 in the Electronic Supplementary Material (ESM)). The obtained Mg_2Si showed the regular bulky morphology (Fig. S2 in the ESM). $ZnCl_2$ not only participated the reaction process of Mg_2Si, but also provided a molten salt condition to improve the reaction efficiency and worked as the medium to inhibit the local high temperature, which may result in the formation of SiC. The reaction can be ascribed as follows

$$Mg_2Si + 2ZnCl_2 = 2MgCl_2 + 2Zn + Si$$

In the product after the reaction, $MgCl_2$, Zn, and unreacted $ZnCl_2$ worked as the templates. The templates were then removed by acid-assisted treatment and the porous morphology can be obtained. To examine the effect of porous morphology of silicon, Si/CNT was also synthesized by directly mixing bulk silicon and CNT directly without further process.

The morphology and structure of as-obtained p-Si/CNT is revealed using FESEM and transmission electron microscope (TEM). Plenty distribution of porous and vacancies can be spotted on the silicon microparticles (Figs. 1(b) and 1(c). TEM images of p-Si/CNT (Figs. 1(d) and 1(e)) further confirmed that the CNTs are uniformly distributed around the porous silicon microparticles and formed a crosslinked matrix. Moreover, high-resolution TEM (HRTEM) image of p-Si/CNT (Fig. 1(f)) also reveals lattice-resolved fringes of 0.31 nm, which agree with (111) plane of crystallized Si. In addition, no distinct lattice fringes are observed from CNT covering on the surface of porous silicon, confirming the amorphous nature of CNTs. The selected area electron diffraction (SAED) pattern (Fig. 1(g)) further suggests the polycrystalline property of porous silicon. Furthermore, the high-angle annular dark field-scanning TEM (HAADF-STEM) images and energy-dispersive X-ray (EDX) elemental mapping were implemented to illustrate the composite structure of p-Si/CNT, as shown in Figs. 1(h) and 1(k).

The phase of the as-prepared p-Si/CNT was obtained by XRD, as shown in Fig. 2(a). The sample exhibits obvious diffraction peaks at 28.4°, 47.3°, 56.1°, 69.1°, and 76.4°, corresponding to planes of crystal Si (111), (220), (311), (400), and (331), respectively (PDF #27-1402) and consistent with HRTEM results mentioned above (Fig. 1(f)). The broad peak spotted at 26.2 can be attributed to the amorphous carbon from the CNTs, which also agrees with the XRD pattern of industrial CNT precursor (Fig. S3 in the ESM). Moreover, no diffraction peaks of Mg_2Si can be

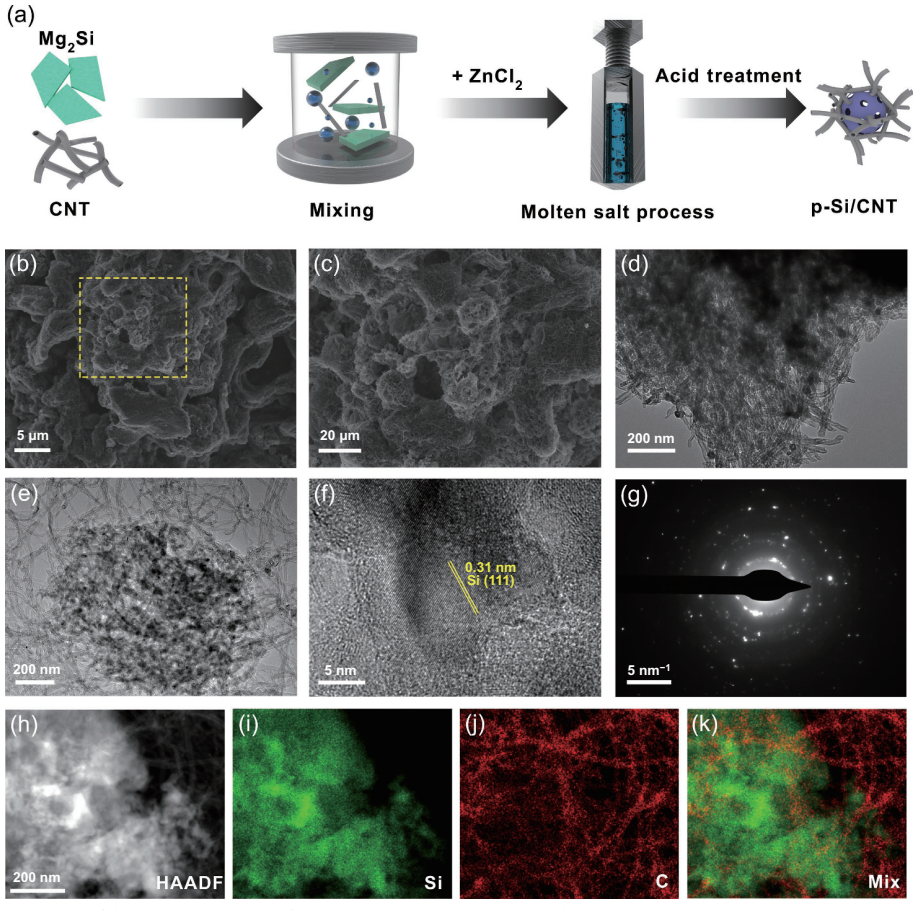

Figure 1 (a) Schematic illustration of the synthesis process of the p-Si/CNT composite, ((b) and (c)) FESEM and ((d) and (e)) TEM images of p-Si/CNT, (f) HRTEM image and corresponding (g) SAED patterns of p-Si/CNT, (h) STEM and ((i)–(k)) EDX elemental mapping images of p-Si/CNT.

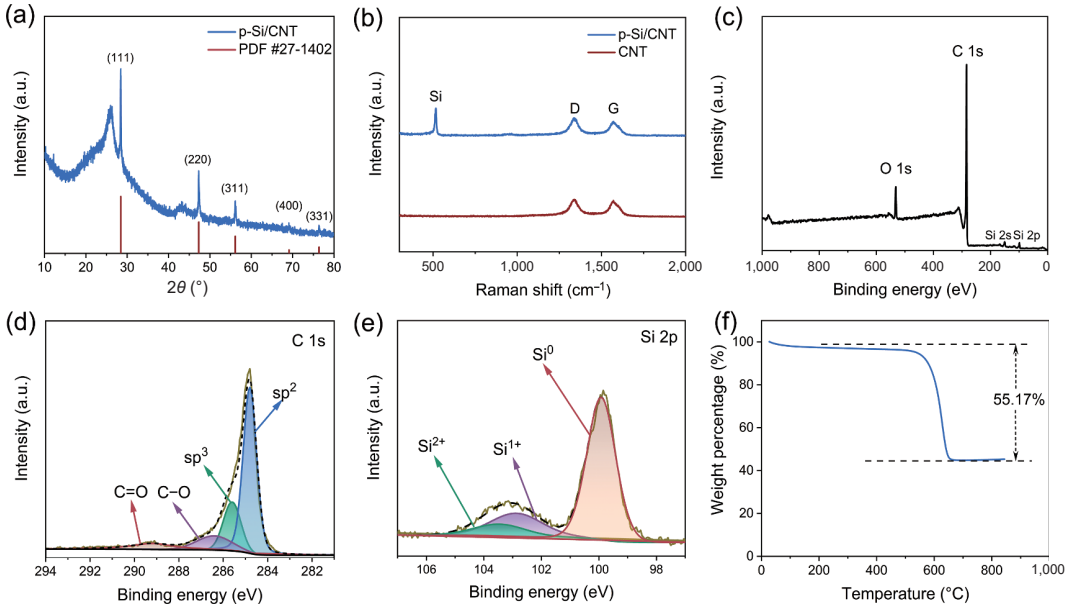

Figure 2 (a) XRD patterns of p-Si/CNT, (b) Raman spectra of p-Si/CNT and pristine CNT, (c) XPS survey of p-Si/CNT, ((d) and (e)) high-resolution C 1s and Si 2p spectra of p-Si/CNT, and (f) TGA curve of p-Si/CNT.

identified (Fig. S4 in the ESM), suggesting that the Mg_2Si was completed consumed under the experimental conditions. Raman spectra of p-Si/CNT and CNTs from 200–2,000 cm^{-1} are presented in Fig. 2(b). The peaks at 518 cm^{-1} reflect the characteristic peak of Si and the peaks at around 1,360 and 1,580 cm^{-1} are ascribed to the D-band and G-band of carbonaceous contents [37]. For p-Si/CNT, I_D/I_G = 1.25 indicates a higher defective carbon content than commercial CNTs (1.09), implying that more carbon defective sites are generated during the molten salt process. The surface composition of obtained p-Si/CNT is further examined by XPS. The full survey of XPS spectrum (Fig. 2(c)) confirms the existence of Si, C, and O elements. The high-resolution C 1s spectrum (Fig. 2(d)) can be split into four peaks at 284.8, 285.6, 286.4, and 289.0 eV, which are attributed to C–C (sp^2), defect peak (sp^3), C–O, and C=O, respectively. Furthermore, Fig. S5 in the ESM also suggests that the ratio of sp^3 defect peak in pristine CNT is lower. Hence, it can be proved that the defect sites in the CNTs increase after the molten salt process. Furthermore, no bonds of Si–C can be spotted [38]. According to the fitting curve of Si 2p spectrum, the signals at 99.8, 102.8, and 103.5 eV (Fig. 2(e)) are analyzed to come from Si^0, Si^{1+}, and Si^{2+}, respectively [39]. Such results indicate the valance of porous silicon and only small amount of silica presents in the as-prepared sample. The quantification of CNT content was determined by TGA, as shown in Fig. 2(f). The carbon content of p-Si/CNT is approximately 55.17 wt.%, which is similar to that of Si/CNT. The porous properties of p-Si/CNT and Si/CNT are analyzed by N_2 adsorption/desorption isotherms, and pore size distribution, as illustrated in Figs. S6 and S7 in the ESM. From the calculation of the isotherms, p-Si/CNT exhibits a high Brunauer–Emmett–Teller (BET) surface area of 126 $m^2 \cdot g^{-1}$, higher than that of Si/CNT (67 $m^2 \cdot g^{-1}$). Given the similar carbon content of p-Si/CNT and Si/CNT, the significant higher surface area of p-Si/CNT is largely attributed to the abundant pore distribution of porous silicon. The average pore size distribution of both p-Si/CNT and Si/CNT is around 2 nm. Moreover, the pore volume of around 30 nm of p-Si/CNT is slightly higher than that of Si/CNT, indicates that both porous silicon and CNT contribute to the high surface area of the composites, and the pore size distribution of the composites is mainly controlled by CNT content. Large surface area and high porosity of the material can benefit the penetration of the electrolyte, which enhances the reaction stability upon electrochemical cycles [40].

The electrochemical lithium storage performance of p-Si/CNT and Si/CNT was evaluated by assembling CR2016 coin-type half cells. Figure 3(a) shows the initial five cycles of CV plots for p-Si/CNT electrode with a voltage range of 0.01–1.5 V (vs. Li^+/Li). In the initial cathodic process, a broad peak at around 0.8 V is corresponding to the formation of SEI, which vanishes in the following cycles. The reduction peak below 0.1 V in the first cycle indicates the alloying reaction between silicon and lithium. This peak is shifted to around 0.2 V in the following cycles. According to previously reported studies, this shift is ascribed to the amorphization process of the crystallized Si during repeating cycles. In the anodic process, the peak at 0.31 and 0.47 V in the anodic process can be ascribed as the dealloying of the Li_xSi alloy. Compared to the anodic peaks in reports of bare silicon [41, 42], the p-Si/CNT exhibits a less polarization during the electrochemical cycles. Furthermore, the well overlapping curves form the second cycles suggest the remarkable reversibility upon alloying and dealloying process of Si and Li_xSi. The increase of the anodic peaks also reveals that the composites may require an activation process due to the porous property. Figure 3(b) shows the typical galvanostatic discharge/charge curves of p-Si/CNT under the current density of 100 $mA \cdot g^{-1}$. The p-Si/CNT electrode delivers initial discharge/charge capacities of 1,841.4 and 973 $mAh \cdot g^{-1}$, corresponding to an initial Columbic efficiency (ICE) of 52.8%. Low ICE is pertaining to the excess formation of SEI due to the high surface area and mesoporous structure of the composite, since the adequate penetration of electrolyte also facilitates the decomposition of electrolyte during the initial cycles. Therefore the pre-lithiation process before the full-cell assembly is an appropriate solution [43]. Figure 3(c) exhibits the cyclic performance of p-Si/CNT at the current density of 500 $mA \cdot g^{-1}$. The current density of initial five cycles was minimized to 100 $mA \cdot g^{-1}$ in order to conduct the activation process. The capacity of p-Si/CNT can be retained at 796.6 $mAh \cdot g^{-1}$ after 100 cycles with CE of approximately 100% and a capacity retention of 78%. Moreover, the rate capability of p-Si/CNT and Si/CNT electrodes was also evaluated in the range of 0.2–10 $A \cdot g^{-1}$, as shown in Fig. 3(d). The p-Si/CNT electrode retains the discharge capacity of 1,202.3, 1,059.9, 877.3, 665.9, 532.4, 387.2, and 339.5 $mAh \cdot g^{-1}$ as the current density increases from 0.2 to 0.5, 1, 2, 3, 5, and 10 $A \cdot g^{-1}$, respectively. Remarkably, after the high rate

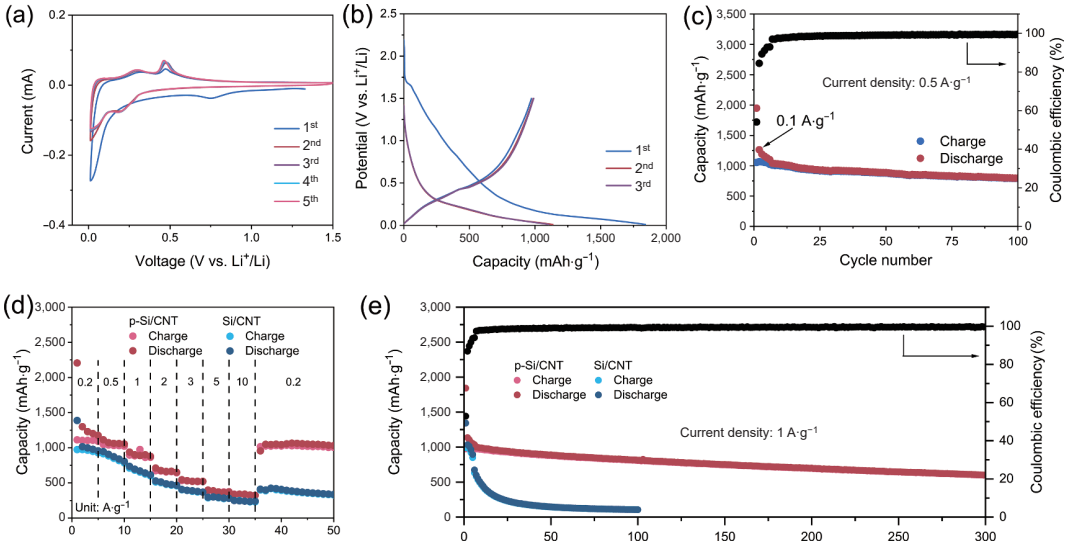

Figure 3 Lithium storage properties of p-Si/CNT. (a) CV curves of p-Si/CNT, (b) charge/discharge voltage profiles of p-Si/CNT, (c) cycling performance of p-Si/CNT at 0.5 A·g^{-1} and the corresponding CE, (d) rate capability of p-Si/CNT and Si/CNT, (e) cycling performance of p-Si/CNT and Si/CNT at 1 A·g^{-1} and the corresponding CE.

cycling at 10 A·g^{-1}, the discharge capacity of 1,015.2 mA·g^{-1} can be restored when the current density is returned to 0.2 A·g^{-1}. In contrast, Si/CNT electrode exhibits an inferior rate capability and poor capacity retention compared to p-Si/CNT electrode, indicating that p-Si/CNT shows a better rate performance. Moreover, the corresponding voltage–capacity profiles of p-Si/CNT electrode (Fig. S8 in the ESM) indicate no obvious polarization as the current density rises to 10 A·g^{-1}. The cycling performance of both electrodes at a high current rate of 1 A·g^{-1} with long cycles was also evaluated, as shown in Fig. 3(e). p-Si/CNT maintains a reversible capacity of 600.5 mAh·g^{-1} up to 300 cycles with the stable CE of approximate 100% and high-capacity retention of 60.1% based on the initial cycle after activation process at 0.2 A·g^{-1}. Moreover, when compared with reported Si/CNT based composite anode, p-Si/CNT also suggested competitive cycle performance and stability (Table S1 in the ESM). In comparison, the Si/CNT electrode not only offers a lower capacity of 105.7 mAh·g^{-1} after 100 cycles, but also a poor capacity retention of 15.7%. To better understand why the p-Si/CNT composite shows such enhanced electrochemical performance, the EIS measurements were carried out for cycled p-Si/CNT and Si/CNT electrode, as shown in Fig. 4(a). Both plots consist of a depressed semicircle in the high frequency region and a straight line in the low frequency region. The diameter of the semicircle corresponds to the charge transfer impedance and the linear region is ascribed to the lithium-ion diffusion of the electrodes. It can be found that the charge transfer impedance of p-Si/CNT is lower than the Si/CNT electrode, which also meets the results of rate capability and cyclic performance shown in Figs. 4(d) and 4(e). The result displays that the participation of CNT matrix enhances the charge transfer kinetics and improves the electrochemical performance of p-Si/CNT anode during lithium insertion/extraction.

To further explore lithium storage mechanism of p-Si/CNT, CV measurements at various sweep rates from 0.1 to 1 mV·s^{-1} are applied, as shown in Fig. 4(b). The redox peak in the profiles can be clearly observed with similar shapes, indicating the stable reaction between Li and Si. As it is well known, the general lithium storage mechanism includes ionic diffusion contribution and capacitive contribution [44]. The capacitive contribution and

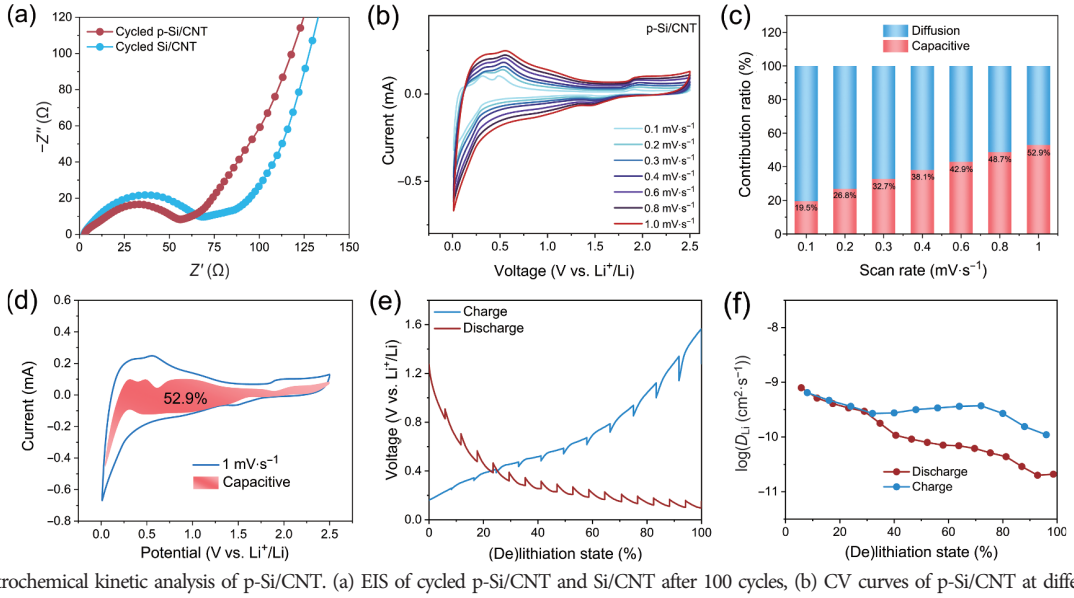

Figure 4 Electrochemical kinetic analysis of p-Si/CNT. (a) EIS of cycled p-Si/CNT and Si/CNT after 100 cycles, (b) CV curves of p-Si/CNT at different scan rates from 0.1 to 1.0 mV·s^{-1}, (c) capacity contribution ratios at various scan rates, and (d) capacitive contribution at 1.0 mV·s^{-1}. (e) The charge and discharge profiles in GITT measurements of the 2nd cycle. (f) The corresponding Li^+ diffusivity coefficient.

diffusion contribution under a fixed potential can be quantitatively determined by the equation: $i = k_1v + k_2v^{1/2}$ where k_1v and $k_2v^{1/2}$ represent the capacitive and diffusion-controlled contribution, respectively. The proportion of two mechanisms can be distinguished by calculating the values of k_1 and k_2. Figure 4(c) reveals that the capacitive contribution of p-Si/CNT electrode can be calculated as 19.5%, 26.8%, 32.7%, 38.1%, 42.9%, 48.7%, and 52.9% at the scan rates of 0.1, 0.2, 0.3, 0.4, 0.6, 0.8, and 1.0 mV·s^{-1}, respectively, which suggests that the capacitive contribution plays a significant role in the electrochemical behavior, especially at the low scan rates. When the sweep rate increases, the capacitive contribution is further improved, and the diffusion-controlled proportion is decreased accordingly, which suggests an increased capacitance-controlled capacity. Figure 4(d) shows the capacitive contribution (red region) in comparison with the total current at the typical scanning speed of 1.0 mV·s^{-1}. A quantitative capacitive contribution of about 52.9% is calculated for p-Si/CNT anode, which suggests a mixed cycling mechanism involving both diffusion and capacitive controlled behaviors. The capacitive contribution under high scan rate may be attributed to the abundant distribution of CNT in the electrode and the high surface area of porous silicon. The solid-state diffusion dynamics of p-Si/CNT electrode is further discussed by galvanostatic intermittence titration technique (GITT) and the corresponding charge and discharge profiles are shown in Fig. 4(e). According to the calculated results in Fig. 4(f), the Li^+ diffusion coefficient values (D_{Li^+}) of p-Si/CNT are ~ 10^{-9}–10^{-11} cm^2·s^{-1} during the second charge and discharge process, which is competitive to the reported silicon-based anodes [35–47]. A relatively stable distribution of the D_{Li^+} plots could be observed during the whole electrochemical cycle, suggesting the fast and stable diffusion behaviors of Li^+ into/from the electrode, which could be attributed to the shortened charge transfer pathways provided by porous Si microparticles within in the CNTs networks.

As mentioned previously, the defects in carbon lattices are increased after the combination with porous Si microparticles. To further probe the mechanism of enhanced cycling performance of defect-rich carbon nanotubes, DFT stimulation of the interaction between defective carbon and lithium atom was performed [48]. Considering no atoms doped, the defect was reasonably speculated to be vacancies. We constructed the models of pristine graphene and defective graphene with single vacancy, as shown in Fig. 5(a). The results indicate that the interaction of Li atom with defective graphene (–3.31 eV) is significantly stronger than that with pristine graphene (–1.65 eV). Furthermore, defective graphene displays the shorter distance between Li atom and carbon atom (2.03 Å) compared to the pristine graphene (2.25 Å), proving that defective graphene possesses the better ability to capture lithium atoms. Collectively, the defects in CNTs could enhance the adsorption of Li^+, which further benefits the electrochemical kinetics during cycling [49, 50].

To further verify the potential of practical application of p-Si/CNT in LIBs, the full cells were assembled by using commercial LCO as cathode. The Li//LCO half cells were first tested, as shown in Fig. S9 in the ESM. The LCO cathode exhibits a reversible capacity of 115 mAh·g^{-1} with a potential plateau at around 3.93 V. In order to reduce the loss of Li and take the full advantage of LCO, before the assembly of full cell, p-Si/CNT was first prelithiated in the half cell for 3 cycles at 0.1 A·g^{-1} [43]. Figure 5(b) displays the initial 3 galvanostatic charging/discharging profiles of p-Si/CNT//LCO full cell at 0.1 C (1 C = 145 mA·g$^{-1}_{LCO}$). Based on the mass of LCO applied, the full cell suggests an initial charge capacity of 169.4 mAh·g^{-1} with an ICE of 70.7% and a potential plateau at 3.86 V. Figure 5(c) shows the cycling performance of p-Si/CNT//LCO full cell. It maintains at 94.3 mAh·g^{-1} at current density of 1 C after 200 cycles. Figures 5(d) and 5(e) show the rate capability of the p-Si/CNT//LCO full cell with discharge capacities of 128, 112, 99, 85, and 70 mAh·g^{-1} at 0.1, 0.2, 0.5, 1, and 2 C, respectively. When the rate abruptly returns to 0.2 C, the full cell is able to recover a reversible capacity of 108 mAh·g^{-1}. Furthermore, the assembled p-Si/CNT//LCO pouch cell is also able to light up a group of light-emitting diodes (LEDs) to form a pattern of "Li–Si" as shown in Fig. 5(f).

In order to quantify the swelling suppressing effect of the porous structure of silicon and carbon nanotubes, the FESEM technique was applied to detect the p-Si/CNT and Si/CNT electrode. Figures S10 and S11 in the ESM show the images of fresh Si/CNT and p-Si/CNT electrodes, respectively. Both electrodes show a uniform distribution of materials on the surface of current collector. Figure 6(a) suggests the surface of Si/CNT electrode after 100 cycles at 1 A·g^{-1} and evident cracks can be observed on the surface due to the serious volumetric variation upon cycling. In contrast, p-Si/CNT electrode maintains its structural integrity with no obvious cracks spotted on the surface

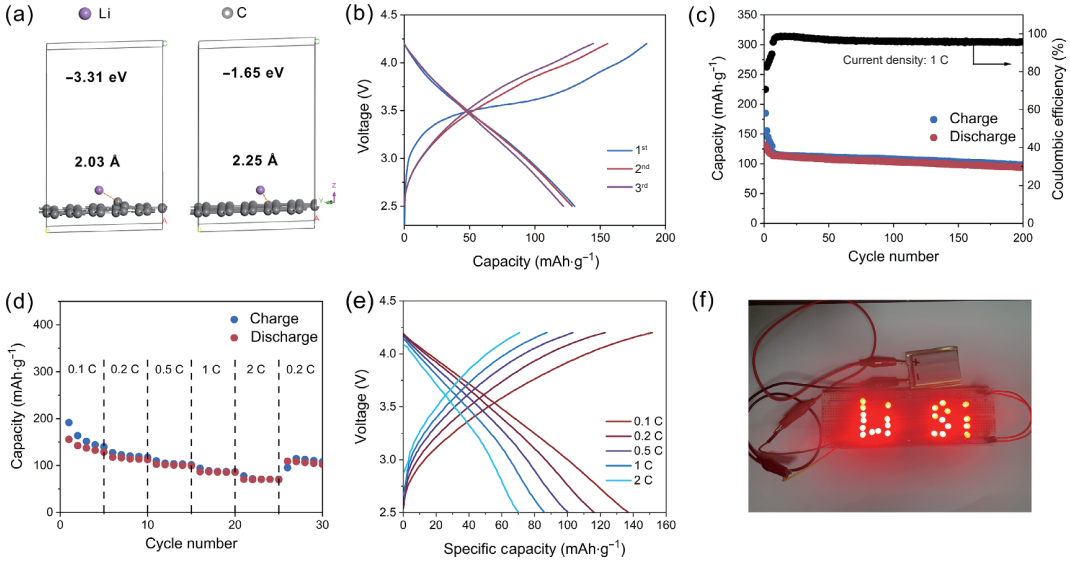

Figure 5 (a) The structural geometry and the schematics of Li conformations on defective graphene with single vacancy and pristine graphene, (b) initial three charge/discharge voltage profiles of p-Si/CNT//LCO full cell, (c) cycling capability and Coulombic efficiency of p-Si/CNT//LCO full cell, (d) rate capability and (e) corresponding charge/discharge voltage profiles of p-Si/CNT//LCO full cell, and (f) a digital image of the p-Si/CNT//LCO pouch full cell lighting up a group of LEDs forming a pattern of "Li–Si".

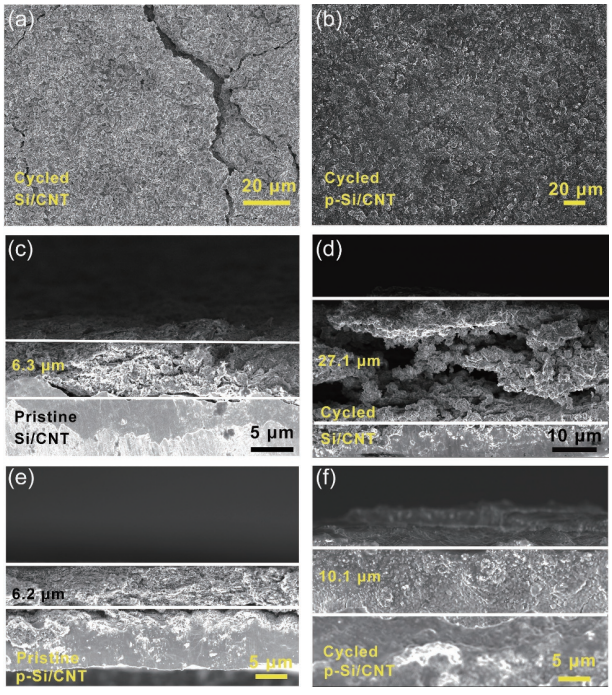

Figure 6 FESEM images of the top surfaces of (a) Si/CNT and (b) p-Si/CNT electrodes after 100 cycles. FESEM images of the cross sections of (c) fresh and (d) cycled Si/CNT electrodes. FESEM of the cross sections of (e) fresh and (f) cycled p-Si/CNT.

of the electrode (Fig. 6(b)). The cross sectional views of Si/CNT and p-Si/CNT are also investigated, as shown in Figs. 6(c)–6(f). The thickness of Si/CNT electrode varies from 6.3 to 27.1 μm (Figs. 6(c) and 6(d)), corresponding to a volumetric expansion of 430%. Furthermore, severe detachment of electrode material from the current collector can also be clearly observable. On the contrary, the thickness of p-Si/CNT expands from 6.2 to 10.1 μm (Figs. 6(e) and 6(f)) with a lower volume variation of 162%. The comparative results notably show us that the porous silicon could significantly provide abundant spare space inside the electrode, dispersively accommodate the stress of the active material upon cycling. In such way, the fracture of electrodes can be effectively buffered.

4 Conclusions

In summary, we develop a simple and low-temperature approach to synthesize microsized porous silicon/carbon nanotubes composite via a molten salt assisted dealloying process. The $ZnCl_2$ molten salt not only improved the efficiency of the reaction and prevented from the formation of electrochemically inactive SiC phase, but also generated more defect sites in lattices of CNTs, which benefited the ion diffusion kinetics confirmed by DFT calculations. The rationally designed p-Si@CNT can efficiently buffer volume change of Si with a stable electrolyte/electrode interface. The p-Si@CNT showed a stable cycling property with 60% capacity retention at 1 $A{\cdot}g^{-1}$ over 300 cycles. Quantitative kinetics analysis disclosed the capacitance-battery dual-model mechanism. The p-Si/CNT//LCO full cell measurement also confirms its potential of commercial applications. The preparation strategy presented here could encourage further capability on precise synthesis of novel architectures with more simple, lower cost, and higher energy conservation.

Acknowledgements

The authors gratefully acknowledge the financial supports provided by the National Natural Science Foundation of China (Nos. U21A2077, 21971145, and 21871164), the Taishan Scholar Project Foundation of Shandong Province (No. ts20190908), the Natural Science Foundation of Shandong Province (Nos. ZR2021ZD05 and ZR2019MB024), and Young Scholars Program of Shandong University (No. 2017WLJH15).

Electronic Supplementary Material: Supplementary material (additional characterization results) is available in the online version of this article at https://doi.org/10.1007/s12274-022-4275-9.

References

[1] Liu, J.; Bao, Z. N.; Cui, Y.; Dufek, E. J.; Goodenough, J. B.; Khalifah, P.; Li, Q. Y.; Liaw, B. Y.; Liu, P.; Manthiram, A. et al. Pathways for practical high-energy long-cycling lithium metal batteries. *Nat. Energy* **2019**, *4*, 180–186.

[2] Zu, C. X.; Yu, H. G.; Li, H. Enabling the thermal stability of solid electrolyte interphase in Li-ion battery. *InfoMat* **2021**, *3*, 648–661.

[3] Parekh, M. H.; Parikh, V. P.; Kim, P. J.; Misra, S.; Qi, Z. M.; Wang, H. Y.; Pol, V. G. Encapsulation and networking of silicon nanoparticles using amorphous carbon and graphite for high performance Li-ion batteries. *Carbon* **2019**, *148*, 36–43.

[4] Zhang, Q. L.; Xi, B. J.; Xiong, S. L.; Qian, Y. T. Carbon coated SiO nanoparticles embedded in hierarchical porous N-doped carbon nanosheets for enhanced lithium storage. *Inorg. Chem. Front.* **2021**, *8*, 4282–4290.

[5] Wang, L. B.; Lin, N.; Zhou, J. B.; Zhu, Y. C.; Qian, Y. T. Silicon nanoparticles obtained via a low temperature chemical "metathesis" synthesis route and their lithium-ion battery properties. *Chem. Commun.* **2015**, *51*, 2345–2348.

[6] Zhou, J. B.; Liu, X. Y.; Cai, W. L.; Zhu, Y. C.; Liang, J. W.; Zhang, K. L.; Lan, Y.; Jiang, Z. H.; Wang, G. M.; Qian, Y. T. Wet-chemical synthesis of hollow red-phosphorus nanospheres with porous shells as anodes for high-performance lithium-ion and sodium-ion batteries. *Adv. Mater.* **2017**, *29*, 1700214.

[7] Zhang, S. J.; Liu, C.; Wang, H. L.; Wang, H. P.; Sun, J. T.; Zhang, Y. M.; Han, X. P.; Cao, Y.; Liu, S.; Sun, J. A covalent P–C bond stabilizes red phosphorus in an engineered carbon host for high-performance lithium-ion battery anodes. *ACS Nano* **2021**, *15*, 3365–3375.

[8] Liu, X. Y.; Zhang, L.; Liu, Z.; Zheng, Y. P.; Zhao, Y.; Yang, Y. C.; Zhang, Q. L.; Li, S. Y. Alkaliphilic $Cu(OH)_2$ nanowires on copper foam for dendrite-free alkali metal anodes. *J. Alloys Compd.* **2022**, *898*, 162815.

[9] Wei, C. L.; Fei, H. F.; An, Y. L.; Tao, Y.; Feng, J. K.; Qian, Y. T. Uniform Li deposition by regulating the initial nucleation barrier via a simple liquid-metal coating for a dendrite-free Li-metal anode. *J. Mater. Chem. A* **2019**, *7*, 18861–18870.

[10] Feng, X. Y.; Wu, H. H.; Gao, B.; Świętosławski, M.; He, X.; Zhang, Q. B. Lithiophilic N-doped carbon bowls induced Li deposition in layered graphene film for advanced lithium metal batteries. *Nano Res.* **2022**, *15*, 352–360.

[11] Sun, Y. M.; Liu, N.; Cui, Y. Promises and challenges of nanomaterials for lithium-based rechargeable batteries. *Nat. Energy* **2016**, *1*, 16071.

[12] Hou, G. L.; Cheng, B. L.; Yang, Y. J.; Du, Y.; Zhang, Y. H.; Li, B. Q.; He, J. P.; Zhou, Y. Z.; Yi, D.; Zhao, N. N. et al. Multiscale buffering engineering in silicon-carbon anode for ultrastable Li-ion storage. *ACS Nano* **2019**, *13*, 10179–10190.

[13] Chen, M.; Zhou, Q. N.; Zai, J. T.; Iqbal, A.; Tsega, T.; Dong, B. X.; Liu, X. J.; Zhang, Y. C.; Yan, C. Y.; Zhao, L. et al. High power and stable P-doped yolk–shell structured Si@C anode simultaneously enhancing conductivity and Li^+ diffusion kinetics. *Nano Res.* **2021**, *14*, 1004–1011.

[14] Han, Y.; Zhou, J.; Li, T. Q.; Yi, Z.; Lin, N.; Qian, Y. T. Molten-salt chemical exfoliation process for preparing two-dimensional mesoporous Si nanosheets as high-rate Li-storage anode. *Nano Res.* **2018**, *11*, 6294–6303.

[15] Zhao, Y. M.; Yue, F. S.; Li, S. C.; Zhang, Y.; Tian, Z. R.; Xu, Q.; Xin, S.; Guo, Y. G. Advances of polymer binders for silicon-based anodes in high energy density lithium-ion batteries. *InfoMat* **2021**, *3*, 460–501.

[16] Tian, Y.; An, Y. L.; Feng, J. K. Flexible and freestanding silicon/MXene composite papers for high-performance lithium-ion batteries. *ACS Appl. Mater. Interfaces* **2019**, *11*, 10004–10011.

[17] Lin, N.; Han, Y.; Zhou, J.; Zhang, K. L.; Xu, T. J.; Zhu, Y. C.; Qian, Y. T. A low temperature molten salt process for aluminothermic reduction of silicon oxides to crystalline Si for Li-ion batteries. *Energy Environ. Sci.* **2015**, *8*, 3187–3191.

[18] Zong, L. Q.; Zhu, B.; Lu, Z. D.; Tan, Y. L.; Jin, Y.; Liu, N.; Hu, Y.; Gu, S.; Zhu, J.; Cui, Y. Nanopurification of silicon from 84% to 99. 999% purity with a simple and scalable process. *Proc. Natl. Acad. Sci. USA* **2015**, *112*, 13473–13477.

[19] Yi, Z.; Qian, Y.; Cao, C. H.; Lin, N.; Qian, Y. T. Porous Si/C microspheres decorated with stable outer carbon interphase and inner interpenetrated Si@C channels for enhanced lithium storage. *Carbon* **2019**, *149*, 664–671.

[20] Sohn, M.; Lee, D. G.; Park, H. I.; Park, C.; Choi, J. H.; Kim, H. Microstructure controlled porous silicon particles as a high capacity lithium storage material via dual step pore engineering. *Adv. Funct. Mater.* **2018**, *28*, 1800855.

[21] Ge, M. Y.; Lu, Y. H.; Ercius, P.; Rong, J. P.; Fang, X.; Mecklenburg, M.; Zhou, C. W. Large-scale fabrication, 3D tomography, and lithium-ion battery application of porous silicon. *Nano Lett.* **2014**, *14*, 261–268.

[22] An, W. L.; Gao, B.; Mei, S. X.; Xiang, B.; Fu, J. J.; Wang, L.; Zhang, Q. B.; Chu, P. K.; Huo, K. F. Scalable synthesis of ant-nest-like bulk porous silicon for high-performance lithium-ion battery anodes. *Nat. Commun.* **2019**, *10*, 1447.

[23] Zhai, W.; Ai, Q.; Chen, L. N.; Wei, S. Y.; Li, D. P.; Zhang, L.; Si, P. C.; Feng, J. K.; Ci, L. J. Walnut-inspired microsized porous silicon/graphene core–shell composites for high-performance lithium-ion battery anodes. *Nano Res.* **2017**, *10*, 4274–4283.

[24] Yi, Z.; Lin, N.; Xu, T. J.; Qian, Y. T. TiO_2 coated Si/C interconnected microsphere with stable framework and interface for high-rate lithium storage. *Chem. Eng. J.* **2018**, *347*, 214–222.

[25] An, Y. L.; Tian, Y.; Wei, H.; Xi, B. J.; Xiong, S. L.; Feng, J. K.; Qian, Y. T. Porosity- and graphitization-controlled fabrication of nanoporous silicon@carbon for lithium storage and its conjugation with MXene for lithium-metal anode. *Adv. Funct. Mater.* **2020**, *30*, 1908721.

[26] Chae, S.; Xu, Y. B.; Yi, R.; Lim, H. S.; Velickovic, D.; Li, X. L.; Li, Q. Y.; Wang, C. M.; Zhang, J. G. A micrometer-sized silicon/carbon composite anode synthesized by impregnation of petroleum pitch in nanoporous silicon. *Adv. Mater.* **2021**, *33*, 2103095.

[27] Huang, Y. H.; Luo, J.; Peng, J.; Shi, M. H.; Li, X. X.; Wang, X. Y.; Chang, B. B. Porous silicon-graphene-carbon composite as high performance anode material for lithium ion batteries. *J. Energy Storage* **2020**, *27*, 101075.

[28] Zhou, W. Y.; Lian, Q. H.; Huang, X. K.; Ding, W. Q.; Jiang, C. H.; Zou, Z. M.; Su, X. D. Introducing SiC/C dual-interface on porous silicon anode by a conventional exothermic displacement reaction for improved cycle performance. *J. Power Sources* **2021**, *508*, 230326.

[29] Salvetat, J. P.; Bonard, J. M.; Thomson, N. H.; Kulik, A. J.; Forró, L.; Benoit, W.; Zuppiroli, L. Mechanical properties of carbon nanotubes. *Appl. Phys. A* **1999**, *69*, 255–260.

[30] Zeng, Y. F.; Huang, Y. D.; Liu, N. T.; Wang, X. C.; Zhang, Y.; Guo, Y.; Wu, H. H.; Chen, H. X.; Tang, X. C.; Zhang, Q. B. N-doped porous carbon nanofibers sheathed pumpkin-like Si/C composites as free-standing anodes for lithium-ion batteries. *J. Energy Chem.* **2021**, *54*, 727–735.

[31] Liang, J. W.; Li, X. N.; Hou, Z. G.; Guo, C.; Zhu, Y. C.; Qian, Y. T. Nanoporous silicon prepared through air-oxidation demagnesiation of Mg_2Si and properties of its lithium ion batteries. *Chem. Commun.* **2015**, *51*, 7230–7233.

[32] Kresse, G.; Furthmüller, J. Efficiency of *ab-initio* total energy calculations for metals and semiconductors using a plane-wave basis set. *Comput. Mater. Sci.* **1996**, *6*, 15–50.

[33] Kresse, G.; Furthmüller, J. Efficient iterative schemes for *ab initio* total-energy calculations using a plane-wave basis set. *Phys. Rev. B* **1996**, *54*, 11169–11186.

[34] Blöchl, P. E. Projector augmented-wave method. *Phys. Rev. B* **1994**, *50*, 17953–17979.

[35] Perdew, J. P.; Burke, K.; Ernzerhof, M. Generalized gradient approximation made simple. *Phys. Rev. Lett.* **1996**, *77*, 3865–3868.

[36] Monkhorst, H. J.; Pack, J. D. Special points for Brillouin-zone integrations. *Phys. Rev. B* **1976**, *13*, 5188–5192.

[37] Peng, X. D.; Xiong, C.; Lin, Y. K.; Zhao, C.; Zhao, T. S. Honeycomb-like hierarchical porous silicon composites with dual protection for ultrastable Li-ion battery anodes. *SmartMat* **2021**, *2*, 579–590.

[38] Acres, R. G.; Ellis, A. V.; Alvino, J.; Lenahan, C. E.; Khodakov, D. A.; Metha, G. F.; Andersson, G. G. Molecular structure of 3-aminopropyltriethoxysilane layers formed on silanol-terminated silicon surfaces. *J. Phys. Chem. C* **2012**, *116*, 6289–6297.

[39] Xu, K. Q.; Ben, L. B.; Li, H.; Huang, X. J. Silicon-based nanosheets synthesized by a topochemical reaction for use as anodes for lithium ion batteries. *Nano Res.* **2015**, *8*, 2654–2662.

[40] Yuan, Y.; Chen, Z. W.; Yu, H. X.; Zhang, X. K.; Liu, T. T.; Xia, M. T.; Zheng, R. T.; Shui, M.; Shu, J. Heteroatom-doped carbon-based materials for lithium and sodium ion batteries. *Energy Storage Mater.* **2020**, *32*, 65–90.

[41] Yang, Z. X.; Du, Y.; Hou, G. L.; Ouyang, Y. G.; Ding, F.; Yuan, F. L. Nanoporous silicon spheres preparation via a controllable magnesiothermic reduction as anode for Li-ion batteries. *Electrochim. Acta* **2020**, *329*, 135141.

[42] An, Y. L.; Fei, H. F.; Zeng, G. F.; Ci, L. J.; Xiong, S. L.; Feng, J. K.; Qian, Y. T. Green, scalable, and controllable fabrication of nanoporous silicon from commercial alloy precursors for high-energy lithium-ion batteries. *ACS Nano* **2018**, *12*, 4993–5002.

[43] Li, X. L.; Gu, M.; Hu, S. Y.; Kennard, R.; Yan, P. F.; Chen, X. L.; Wang, C. M.; Sailor, M. J.; Zhang, J. G.; Liu, J. Mesoporous silicon sponge as an anti-pulverization structure for high-performance lithium-ion battery anodes. *Nat. Commun.* **2014**, *5*, 4105.

[44] Simon, P.; Gogotsi, Y.; Dunn, B. Where do batteries end and supercapacitors begin? *Science* **2014**, *343*, 1210–1211.

[45] Pan, K.; Zou, F.; Canova, M.; Zhu, Y.; Kim, J. H. Systematic electrochemical characterizations of Si and SiO anodes for high-capacity Li-Ion batteries. *J. Power Sources* **2019**, *413*, 20–28.

[46] Suh, S.; Choi, H.; Eom, K.; Kim, H. J. Enhancing the electrochemical properties of a Si anode by introducing cobalt metal as a conductive buffer for lithium-ion batteries. *J. Alloys Compd.* **2020**, *827*, 154102.

[47] Zhang, H.; Zong, P.; Chen, M.; Jin, H.; Bai, Y.; Li, S. W.; Ma, F.; Xu, H.; Lian, K. *In situ* synthesis of multilayer carbon matrix decorated with copper particles: Enhancing the performance of Si as anode for Li-ion batteries. *ACS Nano* **2019**, *13*, 3054–3062.

[48] Cai, W. L.; Song, Y. Z.; Fang, Y. T.; Wang, W. W.; Yu, S. L.; Ao, H. S.; Zhu, Y. C.; Qian, Y. T. Defect engineering on carbon black for accelerated Li-S chemistry. *Nano Res.* **2020**, *13*, 3315–3320.

[49] Fan, X. F.; Zheng, W. T.; Kuo, J. L. Adsorption and diffusion of Li on pristine and defective graphene. *ACS Appl. Mater. Interfaces* **2012**, *4*, 2432–2438.

[50] Zheng, J. M.; Ren, Z. Y.; Guo, P.; Fang, L.; Fan, J. Diffusion of Li^+ ion on graphene: A DFT study. *Appl. Surf. Sci.* **2011**, *258*, 1651–1655.